Rogue and solitary waves in coupled phononic crystals

Y. Miyazawa, C. Chong, P. G. Kevrekidis, and J. Yang

Phys. Rev. E **105**, 034202 — Published 14 March 2022

DOI: 10.1103/PhysRevE.105.034202

Rogue and solitary waves in coupled phononic crystals

Y. Miyazawa,[1] C. Chong,[2] P. G. Kevrekidis,[3] and J. Yang[1]

[1]*Department of Aeronautics and Astronautics, University of Washington, Seattle, Washington 98195*
[2]*Department of Mathematics, Bowdoin College, Brunswick, Maine 04011*
[3]*Department of Mathematics and Statistics, University of Massachusetts Amherst, Amherst, Massachusetts 01003-4515*

(Dated: February 9, 2022)

In this work we present an analytical and numerical study of rogue and solitary waves in a coupled one-dimensional nonlinear lattice that involves both axial and rotational degrees of freedom. Using a multiple-scale analysis we derive a system of coupled nonlinear Schrödinger-type equations in order to approximate solitary waves and rogue waves of the coupled lattice model. Numerical simulations are found to agree with the analytical approximations. We also consider generic initialization data in the form of a Gaussian profile and observe that they can result in the spontaneous formation of rogue wave-like patterns in the lattice. The solitary and rogue waves in the lattice demonstrate both energy isolation and exchange between the axial and rotational degrees of freedom of the system. This suggests that the studied coupled lattice has the potential to be an efficient energy isolation, transfer, and focusing medium.

I. INTRODUCTION

Rogue waves are large waves that appear suddenly and disappear without a trace [1]. Ocean rogue waves were first measured in the North Sea several decades ago [2–5] sparking interest in their scientific study. Since then, multiple measurements were conducted elsewhere across the globe [5–7], providing evidence that ocean rogue waves are an important feature worthy of further exploration. According to the statistical maritime definition, rogue waves are localized both in space and time with an amplitude two times larger than the significant wave height [1]. The study of the rogue wave has gone well beyond oceanographic settings, and includes other spatially continuous systems, such as water tanks [8–11], ultra-cold bosonic gases [12], nonlinear optics [13–16], microwave transport [17], and space plasma [18–21]. Indeed, at this point, numerous reviews [22] and books [7, 23] have summarized the rapidly expanding state of the art on the subject.

A central possibility towards the existence of rogue waves, including many of the above themes, involves the nonlinear effects of the underlying system. In particular, in the previously mentioned physical settings the focusing nonlinear Schrödinger equation (NLSE) [24, 25] can be derived as an approximate model under a suitable set of assumptions/approximations. Among the exact solutions of NLSE, the Peregrine soliton solution [26] is considered a prototypical example of a rogue wave, given that it has only one localized peak in the spatio-temporal domain. The peak amplitude is three times larger than the background plane wave amplitude and satisfies the classical maritime definition of the rogue wave. Indeed, not only the Peregrine soliton but even the corresponding higher order (breather) generalizations thereof have been observed in recent experiments [9].

Despite the vast amount of recent activity on the study of rogue waves, there have been relatively few reports on their study in solids or structures, and in the associated spatially discrete models. Only recently, rogue waves in chains of interacting particles (so-called granular crystals) have been numerically and analytically explored [27]. Another example of a discrete setting where rogue waves have been studied is the integrable Ablowitz-Ladik lattice [28], which is known to have an exact solution that has similar properties as the NLSE Peregrine soliton. Rogue waves have also been studied in the discrete Hirota lattice [29, 30] and Salerno lattice [31, 32]. It is interesting to note that in a number of relevant NLSE lattice models, it was recognized that rogue waves are more likely to arise at or near the integrable limit (such as the Ablowitz-Ladik lattice), rather than its non-integrable analogue, e.g., the standard discrete NLSE case [32–34].

At the level of granular systems, the pioneering work of [35] was the firs, to our knowledge, to recognize the potential of such systems for unusually large (rogue) fluctuations in late time dynamics, in the absence of dissipation. Recent work in this direction has, in fact, posited that in Fermi-Pasta-Ulam-Tsingou (FPUT) non-integrable lattices, rogue fluctuations may be generic for sufficiently long times [36].

Models of one-dimensional (1D) lattices that include additional degrees of freedom have also gained significant recent attention [37–44]. For example, the standard model of the granular crystal accounts for axial (translational) motion of the particles but ignores any rotation. Models that account for the additional degree of freedom in the form of rotation have the obvious benefit of being more realistic representations of the physical system, but such models can also lead to other novel dynamics such as rotational-translational modes [37]. Further studies have demonstrated the localized translational-rotational modes in the coupled linear systems [38], which can offer mechanisms for energy transfer from one degree-of-freedom to another by utilizing topologically protected modes [39]. The wave propagation in the linear, multi-degree-of-freedom 1D lattice has also been shown to facilitate the energy spreading [40], or be easily manipulated by tuning the lattice configura-

tion by using one of the degrees of freedom as a control knob in the magneto-granular crystal [41]. By introducing nonlinearity, the linear dispersion relationship can be corrected with nonlinear terms resulting in nonlinear resonances that can significantly enhance the energy harvesting capability of the lattice [42, 44]. The action of nonlinearity may also have significant further implications, such as the existence of amplitude gaps for the existence of traveling (nonlinear) waves [43] in a metamaterial lattice constructed out of LEGO bricks. Another example of a coupled system (which incorporates axial and rotational degrees of freedom) is the origami-inspired mechanical lattice. Recently, it has been shown that rarefaction solitary waves exist in this lattice [45]. Elastic vector solitons with more than two components (e.g., two translational and one rotational) have also been studied recently via combinations of analytical and numerical tools and present a rich phenomenology in their own right, including the potential emergence of focusing, sound bullet-forming events [46].

In the present study, we consider a lattice with two coupled channels (i.e., one that accounts for two sets of degrees of freedom) with a polynomial nonlinearity to explore wave-focusing events, leading to the potential formation of solitary or of rogue waves. The coupling mechanism investigated in this study can either facilitate or prevent the transfer of energy between two modes. For example, we can manage mechanical energy (e.g., energy harvesting, vibration filtering, and impact mitigation) in one mode by imposing a specific initial condition in the other mode. This control mechanism can be potentially useful for multiple degree-of-freedom mechanical setups, which are ubiquitous in engineering systems, such as beams [47–49], plates [47], tensegrity [50–52], and origami [45, 53, 54]. The study of such effects on the general coupled nonlinear lattice may, in fact, be of broader interest to applications not only in engineering fields such as efficient energy transfer and harvesting, but also in other discrete physics platforms, such as granular crystals in substrates [44] and nonlinear DNA dynamics [55–57].

The paper is structured as follows: In Sec. II we introduce the physical setup and corresponding model equations. An analytical approximation is derived in Sec. III by performing a multiple-scale expansion to obtain an NLSE-like system. Section IV summarizes the exact and approximate solitary waves of the derived NLSE, which are used to initialize the simulations of the full lattice model, yielding good agreement between the NLSE-based approximation and the full direct numerical simulation of the original nonlinear lattice system. Sec. V considers simulations with initial data given by the Peregrine solution of the derived NLSE-like system. More general conditions leading to the formation of rogue-wave-like structures are considered in Sec. VI, where simulations starting from (more "generic") Gaussian initial data are used. The energy exchanged between the two channels (i.e., the different degrees of freedom) is quantified in Sec. VII. Section VIII concludes the paper and presents some possible directions for further study.

II. PHYSICAL SETUP AND MATHEMATICAL MODEL

In this study, we consider a lattice consisting of particles with two sets of degrees of freedom: an axial degree of freedom u and a rotational degree of freedom φ. The particles have mass m and rotational inertia j. See Fig. 1(a) for a schematic representation of an example physical system with two sets of degrees of freedom; similar systems can also be found, e.g., in Ref. [39, 45, 58]. The equivalent mass-spring system of Fig. 1(a) is shown in Fig. 1(b), where axial and rotational sets of degrees of freedom are considered separately (see Supplementary Note 1 for more detail). In the mass-spring visualization, there are two one-dimensional lattices composed of lumped masses and inertial discs that are connected to each other via nonlinear springs. Other examples where our model would be relevant include the aforementioned granular crystal [37], Kresling origami [59], and a compliant mechanism [60]. Note, if the coupled nonlinear springs are significantly stiff, the lattice can be considered as a quasi-one degree of freedom system [45].

The coupled lattice is governed by the following equations of motion,

$$m_n\ddot{u}_n = V_1'(\Delta u_{n-1}, \Delta\varphi_{n-1}) - V_1'(\Delta u_n, \Delta\varphi_n), \quad (1a)$$
$$j_n\ddot{\varphi}_n = V_2'(\Delta u_{n-1}, \Delta\varphi_{n-1}) - V_2'(\Delta u_n, \Delta\varphi_n), \quad (1b)$$

where m_n and j_n are the mass and rotational inertia of the axial and rotational component, respectively, $\Delta u_n = u_n - u_{n+1}$ and $\Delta\varphi_n = \varphi_n - \varphi_{n+1}$ are the axial and rotational strains, with u_n and φ_n being the axial displacement and angle of rotation of the n-th particle respectively. V_1' and V_2' are the general nonlinear force and torque terms determined by differentiating the total potential energy $V = V(\Delta u, \Delta\varphi)$ of the unit cell as follows:

$$V_1' = \frac{\partial V}{\partial(\Delta u)}, \quad V_2' = \frac{\partial V}{\partial(\Delta\varphi)}. \quad (2)$$

Here, the total potential energy V is a function of Δu and $\Delta\varphi$, and therefore the Hamiltonian of this system is

$$H = \sum_{n\in\mathbb{Z}} \left[\frac{1}{2}\left(m_n\dot{u}_n^2 + j_n\dot{\varphi}_n^2\right) + V(\Delta u_n, \Delta\varphi_n)\right]. \quad (3)$$

In the present work, we assume that the masses are identical ($m_n = m$ and $j_n = j$), and that the potential V is a fourth-order polynomial, which can be thought of as a Taylor expansion of an application specific potential (e.g., V has the form of a power-law in the case of the precompressed granular crystal lattice [61]). In particular, the total potential energy function V considered here

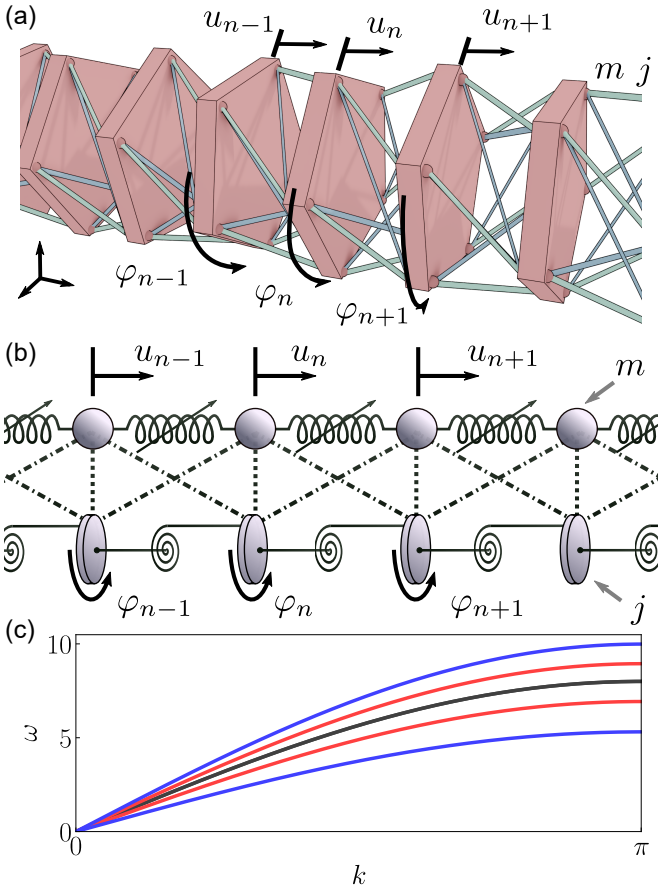

FIG. 1: Schematic of the axial-rotation coupled lattice. (a) Prototypical model of the coupled system. The system consists of plates that have mass m and rotational inertia j, connected through truss-like nonlinear springs. (b) Schematic of the corresponding 1D lattice with two sets of degrees of freedom, which is modeled as a coupled lattice system with lumped mass m and disc with rotational inertia j. The lumped masses are connected with nonlinear springs, and so are the discs. Adjacent masses and discs are connected with nonlinear springs as well, denoted as dashed and dash-dotted lines. (c) The dispersion relationship both with and without the coupling term α_{12}. Black dashed line: $\alpha_{11} = \alpha_{22} = 16$ and $\alpha_{12} = 0$; red solid lines: $\alpha_{11} = 20$, $\alpha_{22} = 12$, and $\alpha_{12} = 0$; blue solid lines: $\alpha_{11} = 20$, $\alpha_{22} = 12$, and $\alpha_{12} = 8$.

is:

$$\begin{aligned} V(x,y) = &\frac{1}{2}\alpha_{11}x^2 + \alpha_{12}xy + \frac{1}{2}\alpha_{22}y^2 \\ &+ \frac{1}{6}\alpha_{111}x^3 + \frac{1}{2}\alpha_{112}x^2y + \frac{1}{2}\alpha_{122}xy^2 + \frac{1}{6}\alpha_{222}y^3 \\ &+ \frac{1}{24}\alpha_{1111}x^4 + \frac{1}{6}\alpha_{1112}x^3y + \frac{1}{4}\alpha_{1122}x^2y^2 \\ &+ \frac{1}{6}\alpha_{1222}xy^3 + \frac{1}{24}\alpha_{2222}y^4. \end{aligned} \tag{4}$$

In the above definition, we assumed nondimensional parameters (note that we retained the same symbols for $u,\ \varphi,\ t$)

$$u_n \to \frac{u_n}{D_0}, \quad \varphi_n \to \frac{R_0\varphi_n}{D_0}, \quad t \to \omega_0 t, \tag{5}$$

where D_0 is the lattice constant, R_0 is the radius of the particle (i.e., of the disc in Fig. 1(b)), and $T_0 = 1/\omega_0 = c\sqrt{m/a_{11}}$ is the characteristic time scale. The parameter c is an arbitrary real constant such that $\alpha_{11} = c^2$ and can be set to any positive real values including $\alpha_{11} = 4$, which we use in the following sections. The a_{11} is the dimensional linear stiffness coefficient of the axial channel (see Supplementary Note 2 for how the nondimensional coefficients α are related to the dimensional coefficients a). With this rescaling, the coupled equations of motion become

$$\ddot{u}_n = V_1'(\Delta u_{n-1}, \Delta\varphi_{n-1}) - V_1'(\Delta u_n, \Delta\varphi_n), \tag{6a}$$
$$\ddot{\varphi}_n = V_2'(\Delta u_{n-1}, \Delta\varphi_{n-1}) - V_2'(\Delta u_n, \Delta\varphi_n). \tag{6b}$$

III. MULTIPLE-SCALE EXPANSION

To analytically explore the behavior of our coupled lattice, we employ asymptotic expansions accompanied with multiple-scale variables [27, 62, 63]. We define the perturbation parameter $0 < \epsilon \ll 1$ and use the perturbative decomposition,

$$\begin{aligned} u_n = &\epsilon\left[A_{1,0} + (A_{1,1}E_n + \text{c.c.})\right] \\ &+ \epsilon^2\left[A_{2,0} + \left(A_{2,1}E_n + A_{2,2}E_n^2 + \text{c.c.}\right)\right] \\ &+ \epsilon^3\left[A_{3,0} + \left(A_{3,1}E_n + A_{3,2}E_n^2 + A_{3,3}E_n^3 + \text{c.c.}\right)\right], \end{aligned} \tag{7a}$$

$$\begin{aligned} \varphi_n = &\epsilon\left[B_{1,0} + (B_{1,1}E_n + \text{c.c.})\right] \\ &+ \epsilon^2\left[B_{2,0} + \left(B_{2,1}E_n + B_{2,2}E_n^2 + \text{c.c.}\right)\right] \\ &+ \epsilon^3\left[B_{3,0} + \left(B_{3,1}E_n + B_{3,2}E_n^2 + B_{3,3}E_n^3 + \text{c.c.}\right)\right], \end{aligned} \tag{7b}$$

where $E_n = E_n(t) = e^{i(kn-\omega t)}$, where k and ω are the wave number and angular frequency, respectively and (c.c.) is the complex conjugate. The $A_{i,j} = A_{i,j}(\xi,\tau)$ and $B_{i,j} = B_{i,j}(\xi,\tau)$ are amplitude functions to be determined that depend on the slow scale variables in space $\xi = \epsilon(n - \lambda t)$ and in time $\tau = \epsilon^2 t$ with λ being the group velocity. This is the usual dispersive scaling that is employed to derive the NLSE and involves considerations of slow spatial scales of size $1/\epsilon$ and slow temporal scales of size $1/\epsilon^2$.

Substituting ansatz (7) into Eq. (6) and collecting the terms according to the order of ϵ yields the wave dispersion relationship $\omega = \omega(k)$ at order $\mathcal{O}(\epsilon^1 E_n^1)$,

$$\begin{aligned} \omega_\pm^2 = 2\left(\alpha_{11} + \alpha_{22} \pm \sqrt{(\alpha_{11} - \alpha_{22})^2 + (2\alpha_{12}\kappa)^2}\right) \\ \times \sin^2\left(\frac{k}{2}\right), \end{aligned} \tag{8}$$

where $\kappa^2 = R_0^2/r^2 = m_n R_0^2/j_n$ is the normalized curvature (i.e., r is a radius of gyration of the disc).

The wave dispersion relationship is shown in Fig. 1(c) for a few selected sets of linear coefficients: α_{11}, α_{12}, and α_{22}. If we keep the coupling term $\alpha_{12} = 0$ and set $\alpha_{22} \neq \alpha_{11}$, this results in two distinct curves denoted as red lines in Fig. 1(c). Similarly, if we let $\alpha_{11} \neq \alpha_{22}$, but now set $\alpha_{12} \neq 0$, the wave dispersion curves appears as two blue curves in Fig. 1(c).

At the order $\mathcal{O}(\epsilon^2 E_n^1)$, we obtain the group velocity $\lambda = d\omega/dk$,

$$\lambda = -\frac{1}{\omega_\pm}\left((\alpha_{11}+\alpha_{22}) \pm \sqrt{(\alpha_{11}-\alpha_{22})^2 + (2\alpha_{12}\kappa)^2}\right) \times \sin k. \tag{9}$$

Note that the group velocity can equivalently also be obtained, by definition, through differentiating the wave dispersion relation (Eq. (8)) with respect to the wave number k [64].

Finally, at order $\mathcal{O}(\epsilon^3 E_n^1)$, nonlinear partial differential equations of $A_{1,1}$ and $B_{1,1}$ emerge,

$$\begin{aligned} &i\partial_\tau A_{1,1} + \nu_2\partial_\xi^2 A_{1,1} + \nu_3\partial_\xi^2 B_{1,1} + \nu_4|A_{1,1}|^2 A_{1,1} + \nu_5|B_{1,1}|^2 B_{1,1} \\ &\quad + \nu_6|B_{1,1}|^2 A_{1,1} + \nu_7|A_{1,1}|^2 B_{1,1} + \nu_8 B_{1,1}^* A_{1,1}^2 + \nu_9 A_{1,1}^* B_{1,1}^2 = 0, \end{aligned} \tag{10a}$$

$$\begin{aligned} &i\partial_\tau B_{1,1} + \mu_2\partial_\xi^2 A_{1,1} + \mu_3\partial_\xi^2 B_{1,1} + \mu_4|A_{1,1}|^2 A_{1,1} + \mu_5|B_{1,1}|^2 B_{1,1} \\ &\quad + \mu_6|B_{1,1}|^2 A_{1,1} + \mu_7|A_{1,1}|^2 B_{1,1} + \mu_8 B_{1,1}^* A_{1,1}^2 + \mu_9 A_{1,1}^* B_{1,1}^2 = 0, \end{aligned} \tag{10b}$$

where superscripts $(^*)$ denote the complex conjugate, and ν and μ with subscripts are the real constant coefficients defined in terms of the coefficients α (see section 3 in the Supplementary Note for more details of the asymptotic expansion and section 4 therein for the detailed expressions of coefficients ν_i, μ_i). Note that Eq. (10) resembles a coupled-NLSE, such as the Manakov system [65]. Unlike the Manakov system, Eq. (10) is non-integrable for generic values of the coefficients ν and μ.

IV. SOLITON INITIAL DATA

To start our investigation, we first consider two special cases where Eqs. (10) reduce to well-known coupled NLSEs. In particular, we consider two representative variants of NLSE, (i) the Manakov system and (ii) the coherently-coupled NLSE with energy exchange term. These special cases have exact solutions, which we use as a reference for the validation of our multi-scale approximation of the lattice dynamics.

A. Manakov Special Case

If we let all NLSE coefficients be zero except for ν_2, μ_3, ν_4, ν_6, μ_7, and μ_5, Eq. (10) reduces to the incoherently-coupled NLSE,

$$i\partial_\tau A_{1,1} + \nu_2\partial_\xi^2 A_{1,1} + \left(\nu_4|A_{1,1}|^2 + \nu_6|B_{1,1}|^2\right) A_{1,1} = 0, \tag{11a}$$

$$i\partial_\tau B_{1,1} + \mu_3\partial_\xi^2 B_{1,1} + \left(\mu_7|A_{1,1}|^2 + \mu_5|B_{1,1}|^2\right) B_{1,1} = 0. \tag{11b}$$

The above equations are generally non-integrable except for a few special sets of coefficients [66–68]. One of these is the well known Manakov system [65]. In this section, we consider the Manakov system with the coefficients $\nu_2 = \mu_3 = 1/2$ and $\nu_4 = \nu_6 = \mu_7 = \mu_5 = 1$, which has exact solutions of the form,

$$\begin{pmatrix} A_{1,1}(\xi,\tau) \\ B_{1,1}(\xi,\tau) \end{pmatrix} = \begin{pmatrix} a(\xi) \\ b(\xi) \end{pmatrix} e^{i2q^2\tau}, \tag{12}$$

where the envelopes a and b are real valued functions (without loss of generality in the 1-dimensional case considered herein), and q is a real parameter associated with the wave frequency. Among the many possible solutions of this form, we consider here the fundamental (bright) one-soliton solutions [25, 65],

$$\begin{pmatrix} a(\xi) \\ b(\xi) \end{pmatrix} = \frac{2q}{\sqrt{P_1^2 + P_2^2}} \begin{pmatrix} P_1 \\ P_2 \end{pmatrix} \operatorname{sech}(2q\xi). \tag{13}$$

Alternatively, if we assume

$$\begin{pmatrix} A_{1,1}(\xi,\tau) \\ B_{1,1}(\xi,\tau) \end{pmatrix} = \begin{pmatrix} a(\xi)e^{i2q_1^2\tau} \\ b(\xi)e^{i2q_2^2\tau} \end{pmatrix}, \tag{14}$$

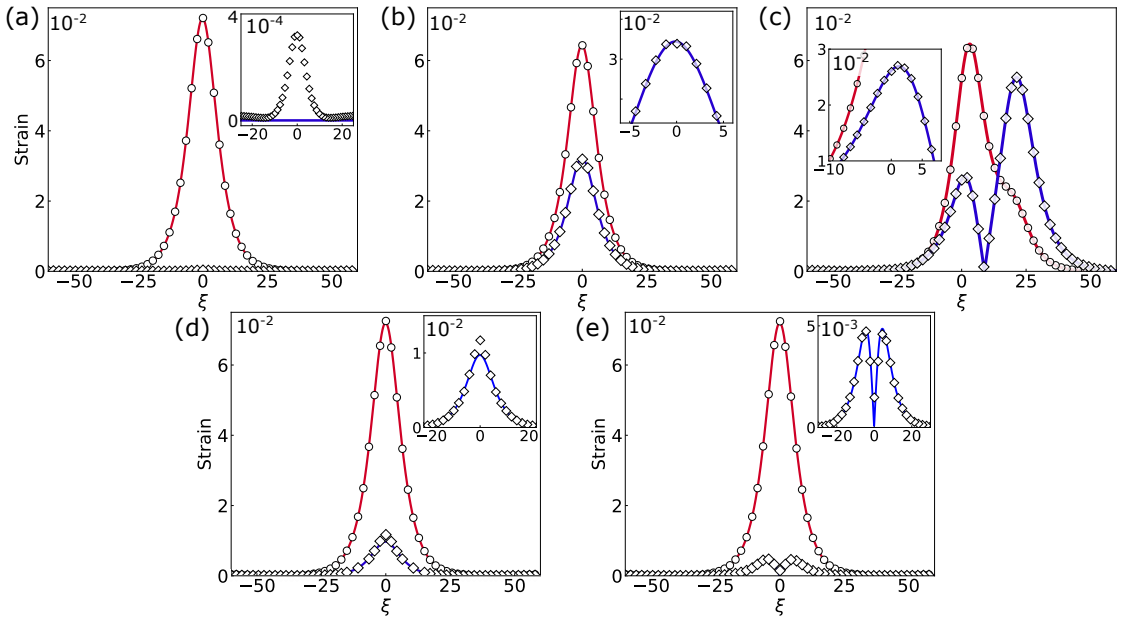

FIG. 2: Coupled soliton solutions, which are analytically predicted (solid lines) and numerically computed for the full lattice equations, Eq. (6), and extracted at $\tau \approx 8$ (open symbols). (a) Initial data given by the single-component soliton of the two-component NLSE model, see Eq. (13) with $P_1 = 1$, $P_2 = 0$, (b) Initial data given by the two-component soliton with different amplitudes, see Eq. (13) with $P_1 = 1$, $P_2 = 0.5$, (c) Initial data given by the incoherently-coupled NLSE soliton with bimodal b component, see Eq. (15), (d) Initial data given by the coherently-coupled NLSE soliton with unimodal b component, see Eq. (17) with $m = 0$, and (e) Initial data given by the coherently-coupled NLSE soliton with bimodal b component, see Eq. (17) with $m = 1$. The parameters are $\epsilon = 0.09$, $\epsilon_1 = 0.027$, $q = 0.1$, $q_1 = 0.1$, and $q_2 = 0.08$. Red solid lines and open circles correspond to the axial mode; blue solid lines and open squares correspond to the rotational mode. All numerical solutions presented are the envelope amplitudes determined via the Hilbert transform. The markers are plotted for every 50 spatial points for better visibility. The insets are zooms of the rotational modes and the markers are plotted for every 25 spatial points.

where two different real frequency parameters q_1 and q_2 exist, Eq. (11) allows the multi-hump soliton solutions [69, 70],

$$\begin{pmatrix} a(\xi) \\ b(\xi) \end{pmatrix} = \frac{2}{F(\xi)} \left[\begin{pmatrix} P_1 e^{2q_1\xi} \\ P_2 e^{2q_2\xi} \end{pmatrix} + g \begin{pmatrix} P_2 q_1^2 e^{2q_2\xi} \\ -P_1 q_2^2 e^{2q_1\xi} \end{pmatrix} e^{2(q_1+q_2)\xi} \right] \tag{15}$$

where P_1 and P_2 are the arbitrary amplitude parameters, $F(\xi) = \frac{P_1^2}{4q_1^2} e^{4q_1\xi} + \frac{P_2^2}{4q_2^2} e^{4q_2\xi} + \frac{P_1^2 P_2^2 (q_1-q_2)^2}{16 q_1^2 q_2^2 (q_1+q_2)^2} e^{4(q_1+q_2)\xi}$, and $g = [P_1 P_2 (q_1 - q_2)]/[(2q_1 q_2)^2 (q_1 + q_2)]$.

B. coherently-coupled NLSE System

Another interesting example where solitary wave solutions can be identified is by setting the coefficients ν_3, ν_5, ν_7, ν_8 and μ_2, μ_4, μ_6, μ_9 of Eq. (10) to zero. Under such a selection, Eq. (10) reduces to the coherently-coupled NLSE [71] with the form:

$$i\partial_\tau A_{1,1} + \nu_2 \partial_\xi^2 A_{1,1} + \left(\nu_4 |A_{1,1}|^2 + \nu_6 |B_{1,1}|^2\right) A_{1,1} + \nu_9 A_{1,1}^* B_{1,1}^2 = 0, \tag{16a}$$

$$i\partial_\tau B_{1,1} + \mu_3 \partial_\xi^2 B_{1,1} + \left(\mu_7 |A_{1,1}|^2 + \mu_5 |B_{1,1}|^2\right) B_{1,1} + \mu_8 B_{1,1}^* A_{1,1}^2 = 0. \tag{16b}$$

Once again, this is a model that frequently arises in nonlinear optics in the realm of processes such as four-wave mixing and a systematic derivation of such models can be found, e.g., in [71].

When $\nu_2 = \mu_3 = 1/2$ and $\nu_4 = \mu_5 = 1$, this system also has solutions of the form given by Eq. (12) [66–68, 71], but now the amplitudes are only approximations,

$$a(\xi) = 2q \,\mathrm{sech}(2q\xi), \tag{17a}$$

$$b(\xi) \approx \epsilon_1 \sqrt{1 - G(\xi)^2}\, {}_2F_1\left(-m, m+3, 2, \frac{1-G(\xi)}{2}\right). \tag{17b}$$

Here, $0 < \epsilon_1 \ll 1$ is another perturbation parameter, $G(\xi) = \tanh(2q\xi)$, and ${}_2F_1$ is a hypergeometric function. In this expression, as is discussed in [71], m is a

non-negative integer, and for each distinct corresponding value a different branch of vector solitons exists. With the constraint that m is an integer, in order for m-th order solitons to exist, the NLSE coefficients require the following relations, $\nu_9 = (m+1)(m+2) - \nu_6, \quad \mu_9 = (m+1)(m+2) - \mu_7$.

C. Numerical simulations of coupled solitons

Figure 2 shows a comparison of analytical and numerical soliton solutions of axial and rotational components. The lattice model shown in Eq. (6) initialized with various soliton solutions of the special cases considered above is numerically solved in the domain $\xi \in [-150, 150]$ and $\tau \in [0, 10]$ with perturbation parameter $\epsilon = 0.09$ (see Supplementary Note 6 for the effect of the choice of ϵ). We employ a Runge-Kutta-Fehlberg method with step size $h = 10^{-4}$ for the time discretization (see Supplementary Note 7 for the numerical error and convergence). Spatial profiles of the analytical and numerical solutions are extracted at $\tau = 8$ (i.e., $t \approx 987.7$), and plotted as solid lines and open symbols, respectively. We choose the lattice coefficients to correspond to the cases considered in Sec. IV(A,B). In particular, for the Manakov case, we used the coefficient values: $\alpha_{11} = \alpha_{22} = 4$, $\alpha_{111} = -1$, $\alpha_{112} = \alpha_{122} = \alpha_{222} = \alpha_{1122} = \alpha_{1222} = 1$, $\alpha_{1111} = \alpha_{2222} = 2$, and $\alpha_{12} = \alpha_{1112} = 0$. For the coherently-coupled case, we used: for $n = 0$, $\alpha_{11} = \alpha_{22} = 4$, $\alpha_{11} = \alpha_{22} = 3$, $\alpha_{112} = 1$, $\alpha_{1111} = 6$, $\alpha_{1112} = \alpha_{1122} = 3/2$, $\alpha_{2222} = 11/2$, and $\alpha_{12} = \alpha_{122} = \alpha_{1112} = 0$. For $n = 1$, $\alpha_{11} = \alpha_{22} = 4$, $\alpha_{111} = 3$, $\alpha_{222} = 19$, $\alpha_{112} = 1$, $\alpha_{1111} = 6$, $\alpha_{1112} = 3/2$, $\alpha_{1122} = 11/2$, $\alpha_{2222} = 363/2$, and $\alpha_{12} = \alpha_{122} = \alpha_{1112} = 0$. Notice that in all the above cases, the leading order coupling term α_{12} is zero, but the lattice is still coupled at higher orders (e.g., $\alpha_{112}u^2$ or $\alpha_{111}u^3$). Although above coefficients are arbitrarily chosen, they are reasonable approximation for a particular setup for the mechanical system in Fig. 1. For some examples, see Supplementary Note 1.

In general, both numerically solved axial and rotational components agree well overall with the analytical approximation, regardless of the initial condition or the choice of coefficients. There are, however, also deviations between the prediction and the actual dynamics, which is to be expected, given the approximate nature of the reduction. For example, there exists a small non-zero solution in the rotational component in Fig. 2(a) (see inset figure), despite initializing the lattice with a single-component solitary wave. This suggests that there is a weak energy leakage from the axial channel (with non-zero initial data) to the rotational channel (with zero initial data). However, given that the spatial profile in rotational mode is very small in amplitude, the relevant energy transfer is rather minimal (see Supplementary Note 8.1 for how this energy leakage varies depending on the strength of the coupling terms).

When we have non-zero amplitude initial data in both axial and rotational components (Fig. 2(b-e)), we see a good agreement with the analytical prediction, even for the case where either or both the axial and rotational component initial condition is asymmetric rather than unimodal (Fig. 2(c) and (e)). There exist some slight disparities in the coherently-coupled NLSE case (i.e., Fig. 2(d-e); see inset figures as well), presumably due to the stronger coupling in the coherently-coupled case (see Supplementary Note 8.2 for how the disparities vary for different values of the coupling coefficients). Nevertheless, the overall agreement is excellent, regardless of the initial condition profile.

V. ROGUE WAVE INITIAL DATA

Next, we consider solutions that are spatio-temporally localized, namely the rogue wave solutions of the two-component NLSE system (Eq. (11)). Again, the NLSE coefficient $\nu_2 = \mu_3 = 1/2$ and $\nu_4 = \nu_6 = \mu_7 = \mu_5 = 1$ are chosen (i.e., the Manakov system).

One of the fundamental rogue wave solutions of the Manakov system [72] is given by

$$\begin{pmatrix} A_{1,1}(\xi,\tau) \\ B_{1,1}(\xi,\tau) \end{pmatrix} = \left[L \begin{pmatrix} P_1 \\ P_2 \end{pmatrix} + M \begin{pmatrix} P_2 \\ -P_1 \end{pmatrix} \right] \frac{e^{i4q^2\tau}}{B}, \tag{18}$$

where a and b are arbitrary real parameters, the real frequency parameter is $q = \sqrt{P_1^2 + P_2^2}$, $L = \frac{3}{2} - 32q^4\tau^2 - 8q^2\xi^2 + i16q^2\tau + |f|^2 e^{4q\xi}$, $M = 4f(2q\xi - i4q^2\tau - \frac{1}{2})e^{2q\xi + i2q^2\tau}$, and $B = \frac{1}{2} + 32q^4\tau^2 + 8q^2\xi^2 + |f^2|e^{4q\xi}$ with f being an arbitrary complex parameter.

Setting $f = 0$, we obtain coupled vector solutions in the axial and rotational components that are reminiscent of the Peregrine soliton. We consider two case examples. One where the axial and rotational components are chosen to be identical (i.e., effectively the single component situation), see Fig. 3(a) and (b). We also consider a case example where the rotational component is 1/10 of the amplitude of the axial component, see Fig. 3(c) and (d). In both cases, the peak amplitude is three times higher than the background and is localized at the origin. There are also density dips in the vicinity of the principal peak.

Using the spatial profile at $\tau = -5$ from the NLSE approximation as initial data, we simulate the lattice dynamics in the domain $\tau \in [-5, 5]$ and $\xi \in [-40, 40]$. The perturbation parameter is set to $\epsilon = 0.09$, and we choose the following coefficients: $\alpha_{11} = \alpha_{22} = 4$, $\alpha_{122} = \sqrt{2}$, $\alpha_{1111} = \alpha_{1122} = 1$, $\alpha_{2222} = 2$, and $\alpha_{12} = \alpha_{111} = \alpha_{112} = \alpha_{222} = \alpha_{1112} = \alpha_{1222} = \alpha_{1222} = 0$. The resulting numerical solutions are shown in Fig. 3(e-h). In both components, the time until the localization coincides well with the analytical prediction, however there are slight discrepancies after the formation of the rogue wave (i.e., $\tau > 0$). In particular, the peak formed at the origin splits into smaller amplitude waves in the lattice case. Similar observations have been made in other lattice settings [27].

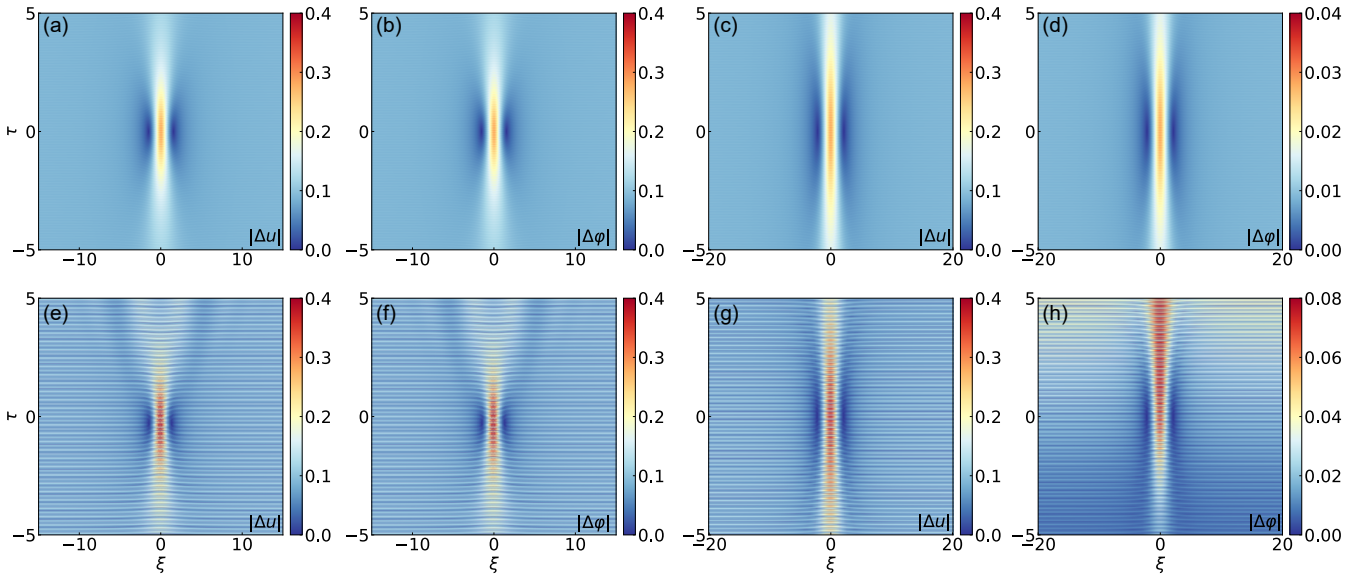

FIG. 3: Coupled rogue wave solutions, which are analytically predicted (top row) and numerically solved for the full lattice equations initialized with Eq. (18) (bottom row). The perturbation parameter is $\epsilon = 0.09$, and the amplitudes are (a,b,e,f) $P_1 = P_2 = 0.2$, $f = 0$, and (c,d,g,h) $P_1 = 0.2$, $P_2 = 0.02$, and $f = 0$.

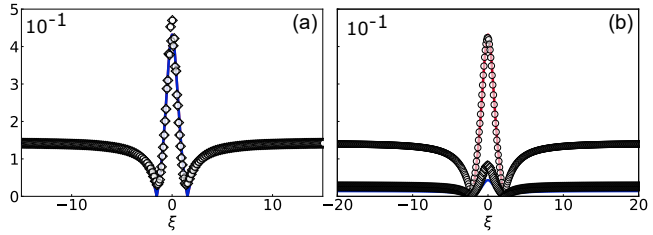

FIG. 4: Spatial profiles of coupled rogue wave solutions extracted at $\tau = 0$ for NLSE (solid lines) and lattice solutions (open symbols) (a) $P_1 = P_2 = 0.2$, $f = 0$, and (b) $P_1 = 0.2$, $P_2 = 0.02$, and $f = 0$. Red lines and circles: axial component; Blue lines and squares: rotational component.

As discussed in Ref. [27], the formation of smaller waves may be induced by the modulational instability of the NLSE background, which is activated due to the large peak amplitude (see Supplementary Note 8.3 for how the deviation from the analytical prediction grows as time evolves).

In Fig. 3(g-h) where the axial and rotational component have different amplitudes, the waves tend to focus and thus localize at the origin. In the axial component, we see that the peak amplitude of the numerical solution is slightly lower than the analytical prediction. On the contrary, the rotational component shows a peak that is twice as high as the analytical prediction. The deviation from the analytical prediction suggests there is energy leakage from the axial component into the rotational component (see Supplementary Note 5 for longer time spatio-temporal evolution and how it differs from analytical prediction). We believe that this is due to the non-zero coupling terms of the lattice equation (e.g., α_{122}), which possibly trigger the energy transfer between two components, in a way that is not reflected in the reduced NLSE system (see Supplementary Note 9 for the effect of coupling terms on the evolution of the coupled rogue wave solution).

VI. GAUSSIAN INITIAL DATA

To further explore rogue wave solutions in the coupled lattice, we hereafter numerically study Eq. (10) in the more general case (i.e., with all coefficients being present). However, as mentioned previously, Eq. (10) is non-integrable, therefore no exact Peregrine-like solution is analytically known. Thus, the lattice cannot be initialized with an analytical prediction to examine the time evolution. As an alternative, we consider more general unimodal shaped data. In particular, we use the Gaussian initialization, which has been shown to be effective in leading to rogue-like waves as a result of the gradient catastrophe phenomenon in the focusing NLSE [73]. This has been mathematically explored originally in the so-called semi-classical continuum NLSE system in the work [73], and more recently explored in corresponding experimental studies in nonlinear optics in the work of [16].

Let the initial data be the Gaussian envelope function [27],

$$\begin{pmatrix} A_{1,1}(\xi, \tau = 0) \\ B_{1,1}(\xi, \tau = 0) \end{pmatrix} = \begin{pmatrix} P_1 \\ P_2 \end{pmatrix} \exp\left(-\frac{\xi^2}{4\sigma^2}\right), \qquad (19)$$

where P_1 and P_2 are arbitrary real parameters that de-

termine the amplitude of the initial profile of $A_{1,1}$ and $B_{1,1}$ respectively, and σ is the width of the localization. The numerical simulation is then conducted in the domain $\tau \in [0, 5]$ and $[0, 20]$, and $\xi \in [-30, 30]$ with the perturbation parameter $\epsilon = 0.09$. The lattice coefficients are set to: $\alpha_{11} = \alpha_{22} = 16$, $\alpha_{12} = 0.016$, $\alpha_{111} = \alpha_{222} = \alpha_{1111} = \alpha_{1112} = \alpha_{1122} = \alpha_{1222} = \alpha_{2222}$, and $\alpha_{112} = \alpha_{122} = 1.6$. Here, these choices are made such that the NLSE becomes the focusing equation (i.e., $\nu_i > 0$ and $\mu_i > 0$). The corresponding simulations of the NLSE (Eq. (10)) are also conducted as a reference solution to be compared with the lattice dynamics solutions. Again, for both lattice and NLSE simulations, we use Runge-Kutta-Fehlberg method with step size $h = 10^{-4}$ and $\eta = 5 \times 10^{-6}$, respectively, for the time discretization of the lattice equation (Eq. (6)) and NLSE (Eq. (10)). The NLSEs are spatially discretized via fourth order central difference scheme with grid size $d\xi = 10^{-2}$. Note that the lattice equation is solved in t domain, and NLSE in τ domain.

Figures 5 and 6 show both lattice and NLSE simulation results for two different cases of initial conditions. Specifically, (i) the initial condition where axial and rotational modes have equal amplitude (i.e., $P_1 = P_2 = 1.0$; Fig. 5), and (ii) the initial condition with the rotational mode being 1/10 of axial mode (i.e., $P_1 = 2.0$, $P_2 = 0.2$; Fig. 6) to examine how the energy transfer differs between the lattice and the NLSE simulation. The localization width $\sigma = 4$ is kept constant between the two cases.

First, if we use the equal amplitude initial conditions, the NLSE creates a tree-like pattern stemming from single peak localization at $\tau \approx 1.1$. This is in line with the integrable NLSE theory of [73] and has also been observed in other systems, both continuum [12] and discrete [27]. The single peak localization has dips on the left and right side, which are directly reminiscent of a Peregrine soliton. In the lattice simulation, we also see the tree-like pattern starting from the peak at $\tau \approx 1.1$, where the single large peak is formed. If we closely examine the peak at $\tau \approx 1.1$, we can see that both the height and width of the peak agree with the NLSE prediction, as can be seen in Fig. 5(e). As can be observed, the branches formed after $\tau \approx 2$ show small differences between the lattice simulation and the NLSE (e.g., the two center peaks are formed slightly later in the lattice spatio-temporal evolution compared to the NLSE and the peak amplitude is different). However, in general, the NLSE and lattice behave in a fairly similar manner, especially from the standpoint of the time at which the wave localizes in the early stage of the time evolution, the formation of the original Peregrine pattern, and also the tree-like pattern that follows.

Similarly, if we employ a smaller amplitude initial condition in the rotational mode, the NLSE and the lattice agree well in their spatio-temporal profiles. In the NLSE simulation, the axial component (Fig. 6(a)), wide Gaussian initial data first decreases and then forms the teardrop-like peak at $\tau \approx 1.01$. This single peak splits

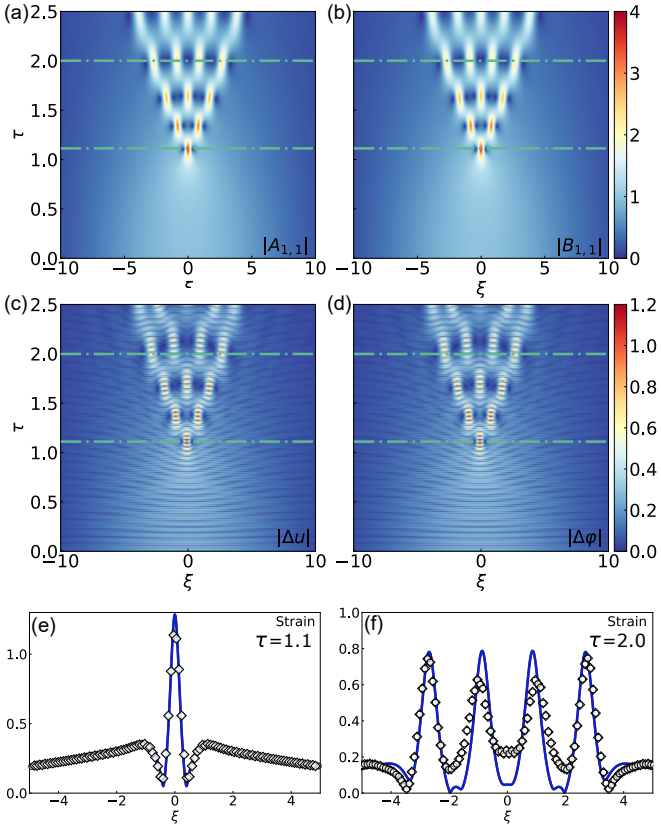

FIG. 5: Numerical solutions of NLSE (a,b) and of the lattice (c,d) with all coefficients in Eq. (10) being non-zero. The perturbation parameter is $\epsilon = 0.09$, the width of the localization is $\sigma = 4$, and the amplitudes are $P_1 = P_2 = 1.0$. Spatial profiles of NLSE and lattice solutions corresponding to the green dash-dotted lines in panel (a-d) for (e) $\tau = 1.1$ and (f) $\tau = 2.0$. Solid lines are the NLSE solutions and open symbols denote the lattice simulation. Red solid lines and open circles: axial component; blue solid lines and open squares: rotational component. Here, NLSE solutions in (e-f) are scaled with ϵ for comparison.

into two peaks at $\tau \approx 1.5$ accompanied by adjacent dips, then into three. In general, the profile develops into a tree-like pattern, similar to the equal amplitude initial data case. As for the rotational component of the NLSE shown in Fig. 6(b), in contrast to the axial component, the amplitude first increases and reaches its highest amplitude at $\tau \approx 0.5$ while keeping the broad width of the Gaussian initial profile. The peak forms slightly earlier than in the axial component case. Similar behavior can be observed for two peaks formed around $\tau \approx 1.2$. As time proceeds, similar to axial component, the single peak splits into two, and then three small peaks. In the lattice solution, we can observe similar dynamics. For instance, the axial component forms a teardrop-like peak at $\tau \approx 1.01$ following the two dips that appears slightly earlier. When these two dips appear in the axial component, the rotational component shows a single peak at $\tau \approx 1.0$. In the spatial profiles of the axial and rotational

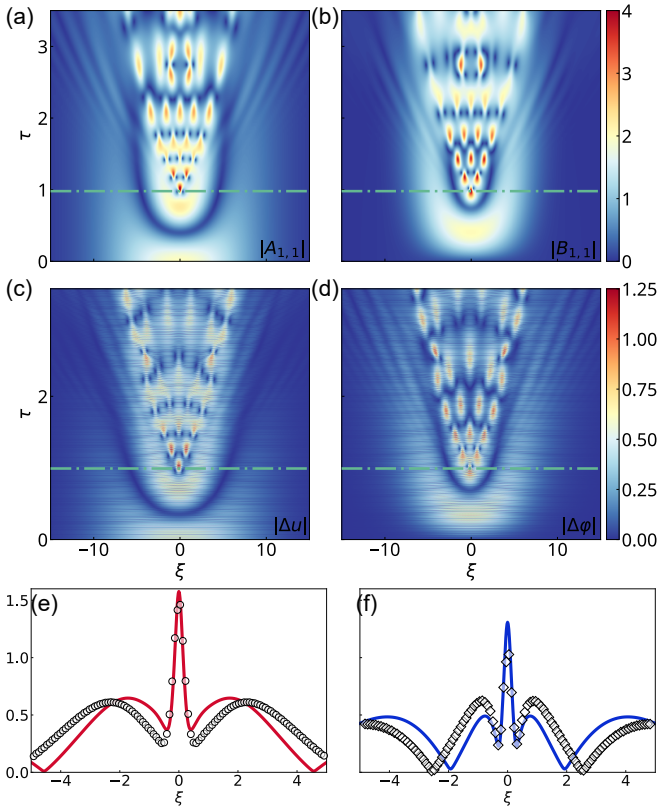

FIG. 6: Numerical solutions of NLSE (a,b) and lattice (c,d) with all coefficients in Eq. (10) being non-zero. Perturbation parameter is $\epsilon = 0.09$, width of the localization is $\sigma = 4$, and the amplitudes are $P_1 = 2.0$, $P_2 = 0.2$. Spatial profiles of the NLSE and lattice solutions corresponding to the green dashed lines in panel (a-d) for (e) $\tau = 2.2$ and (f) $\tau = 8.0$. Solid lines are the NLSE solutions and open symbols denote the lattice simulation. Red solid lines and open circles: axial component; blue solid lines and open squares: rotational component. Here, NLSE solutions in (e-f) are scaled with ϵ for comparison.

component extracted at $\tau = 1.01$ (Fig. 6(e-f)), we see the lattice solution qualitatively matches with the NLSE solution, with some disparities in their width. However, as we also observe in the equal amplitude initial data case, the spatio-temporal evolution of the lattice starts to show large deviation from the NLSE behavior as time proceeds. After $\tau \approx 2$ the pattern formation (e.g., number of peaks) of the lattice significantly deviate from those of NLSE.

VII. ENERGY EXCHANGE

In this section, we revisit the soliton and rogue wave solutions of the lattice simulation studied in the previous sections, and examine the energy profiles in the axial and rotational modes as a function of time. We split the energy into two groups, (i) axial component and (ii) rotational components as follows:

$$E_1 = \frac{1}{2}\dot{u}^2 + \frac{1}{2}\alpha_{11}u^2 + \frac{1}{6}\alpha_{111}u^3 + \frac{1}{24}\alpha_{1111}u^4 + \frac{1}{2}E_{cp}, \tag{20a}$$

$$E_2 = \frac{1}{2}\dot{\varphi}^2 + \frac{1}{2}\alpha_{22}\varphi^2 + \frac{1}{6}\alpha_{222}\varphi^3 + \frac{1}{24}\alpha_{2222}\varphi^4 + \frac{1}{2}E_{cp}, \tag{20b}$$

$$E_{cp} = \alpha_{12}u\varphi + \frac{1}{2}\alpha_{112}u^2\varphi + \frac{1}{2}\alpha_{122}u\varphi^2 + \frac{1}{6}\alpha_{1112}u^3\varphi + \frac{1}{4}\alpha_{1122}u^2\varphi^2 + \frac{1}{6}\alpha_{1222}u\varphi^3. \tag{20c}$$

Note that we evenly distribute the energy due to coupling terms (or energy exchange terms) E_{cp} among E_1 and E_2. We investigate these two energy quantities for the solitary, rogue, and Gaussian induced wave solutions shown in Fig. 2, Fig. 3, and Fig. 6 respectively. Figure 7 shows the energy of the axial and rotational component of different cases of the lattice simulation.

First, we take a closer look at the soliton solution case shown in Fig. 7(a) and (b), which corresponds to the soliton solutions shown in Fig. 2(a) and (c) respectively. In general, both soliton solution energy profiles suggest that the energy does not transfer from one mode to another (i.e., E_1 and E_2 are constant throughout), except for the minimal leakage seen in the inset plot of Fig. 7(a). This energy leakage can also be seen in the spatial profile in Fig. 2(a), where the rotational mode profile has a very small peak at the center. The magnitude of the energy in the rotational mode rapidly increases from zero and then saturates, in this case around $E_2/E_t = 2.5 \times 10^{-5}$, while showing the oscillatory behavior due to the fast time scale dynamics. Indeed, the oscillatory nature of the solution at constant energy preserves the dynamics essentially thereafter. As mentioned earlier, although we set the leading order coupling term $\alpha_{12} = 0$, the lattice of interest is still coupled at higher orders (e.g., $\alpha_{112}u^2$ or $\alpha_{111}u^3$). Therefore, with non-zero axial amplitude u, the rotational mode is excited, and effectively the axial mode plays the role of an external potential of small amplitude, leading to practically linear dynamics in the rotational mode. Nonetheless, the energy leakage remains minimal in this case (the energy leakage can be suppressed by employing weaker coupling coefficients in the lattice while maintaining the validity of the Manakov approximation; see Supplementary Note 8). The profiles in Fig. 7(b) also suggest the suppression of energy leakage since the energy profiles are almost constant, with minimal energy leakage from the axial to rotational the component. In the inset panel of Fig. 7(b), we see that the deviation from the initial value $\frac{E_2 - E_2(0)}{E_t}$ is quite small ($\approx 5 \times 10^{-5}$) and practically negligible (but still far more significant than the numerical errors; see Supplementary Note 7).

In Fig. 7(c) we show the time evolution of the energy component of the coupled rogue wave solution, which corresponds to the strain wave field in Fig. 3(g,h), but with $\tau = 35$. We observe a continual and gradual exchange

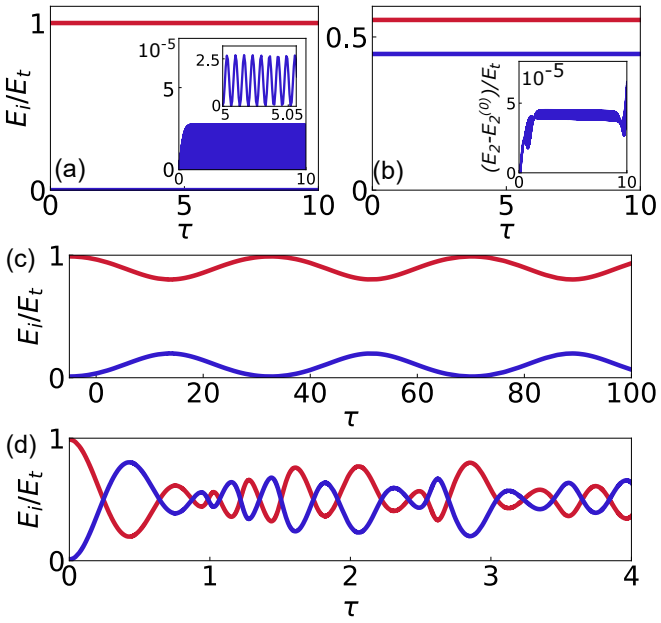

FIG. 7: Energy profiles of axial E_1 and rotational E_2 component of the lattice, normalized by the total energy E_t. Red solid lines, axial component E_1; blue solid lines, rotational component E_2. Each panel corresponds to the soliton solutions: (a) Fig. 2(a), (b): Fig. 2(c), and rogue wave solutions (c): Fig. 3(g-h), and Gaussian initial data solutions (d): Fig. 6(c-d). The inset panels in: (a) represents a magnified view of the rotational mode in $\tau \in [0, 10]$ and $\tau \in [5, 5.05]$; (b) represents the deviation from the initial energy in rotational component, $[E_2 - E_2(0)]/E_t$.

of energy between the two channels. As time progresses, the energy distributed to the rotational component grows and reaches its maximum, which is about 1/4 of the energy in axial component at $\tau \approx 14$. Then, E_2 decreases and attains a minimum at $\tau \approx 32$. Even in the longer term behavior, this gradual and partial exchange of the energy continues in a recurrent manner (see also Supplementary Note 5 for the spatio-temporal evolution).

Finally, we explore the energy exchange between the axial and rotational components of the rogue wave-like solutions induced by Gaussian initial data, shown in Fig. 7(d), which correspond to the strain wave field in Fig. 6. Unlike the above three cases, we see significant energy transfer between the two components. As observed in the spatio-temporal evolution of the lattice solution, the axial and rotational component exchange a significant amount of energy quite quickly. Indeed the rotational component of the energy E_2 overtakes the axial component at $\tau \approx 4.5$. When the first peak forms in the axial component of the lattice simulation ($\tau \approx 1.01$; a narrow peak forms in rotational component), we see that the two energy components become almost identical. Interestingly, even after the single peak formation, when the spatio-temporal profile of the lattice shows peaks, the difference between the two energy component becomes small. For instance, two energy components essentially become identical again, when four peaks become significantly high in amplitude at $\tau \approx 1.8$ in the rotational component (two narrow peaks form in the axial component). Similar behavior can also be observed at $\tau \approx 2.5$ and $\tau \approx 3.6$. (additional analysis in Supplementary Note 8.4 shows how the energy transfer between the two channels depends on the strength of the coupling terms.)

In summary, we observe three qualitatively different types of behavior of energy transfer. For solitary wave initial data, there is minimal transfer of energy. For Peregrine initial data, there is a partial transfer of energy between channels, and for Gaussian initial data, the energy is transferred continually between the two channels in an aperiodic and oscillatory fashion.

VIII. CONCLUSIONS AND FUTURE WORK

In conclusion, we have analytically and numerically explored nonlinear waves in an FPUT lattice with axial and rotational modes involving up to cubic stiffness. We first derived coupled NLSE equations via a multiple-scale analysis. Variants of both incoherently-coupled and coherently-coupled forms were considered and used to approximate the full lattice dynamics. The approximation based on the solitary wave solution of the incoherently-coupled NLSE compared favorably to the numerical simulation of the coupled FPUT lattice, both with and without energy exchange terms. In the coherently-coupled NLSE case, we also explored more complex waveforms in addition to the simplest unimodal solitary wave (where one component played the role of an effective potential for the other). Furthermore, rogue wave type dynamics were studied. First we used the exact coupled rogue wave solution of the incoherently-coupled NLSE system (i.e., Manakov system), as the initial condition. Regardless of the initial profile, the localization time of the analytical and numerical solution matched well, except for the small but noticeable energy leakage from the axial component to the rotational component. When initialized with a sufficiently wide Gaussian envelope function, the lattice showed a clear localization due to the gradient catastrophe phenomenon, accompanied by the formation of secondary peaks, in line with a similar phenomenology previously analyzed in the NLSE realm. Depending on the configuration and the initial data, coupled lattices of the FPUT type considered herein can effectively isolate the energy (e.g., soliton solutions) to one of the modes or continuously exchange the energy between modes while forming a peak (e.g., Gaussian initial data solutions).

We believe that these findings open an analytical window of investigation of a multitude of systems that have recently been explored in various experiments at the multi-component setting [43, 45, 46]. This allows one to observe wave localization in a general coupled discrete nonlinear system, and may, in principle, open avenues to explore energy control in mechanical systems. At the same time, while here we presented the rele-

vant multi-component technique at the one-dimensional, two-component setting, there are various recent works that suggest the relevance of corresponding considerations for higher numbers of components [46] or higher dimensions [74].

Acknowledgements

The present paper is based on work that was supported by the US National Science Foundation under Grant Nos. CAREER-1553202 and CMMI-1933729 (JK), DMS-1809074 (PGK) and DMS-1615037 and DMS-2107945 (CC). Y.M. and J.Y. are grateful for the support of the Washington Research Foundation.

[1] C. Kharif and E. Pelinovsky, European Journal of Mechanics - B/Fluids **22**, 603 (2003).
[2] S. Haver, Rogue waves 2004 : proceedings of a workshop organized by Ifremer and held in Brest, France **2004**, 1 (2004).
[3] D. A. Walker, P. H. Taylor, and R. E. Taylor, Applied Ocean Research **26**, 73 (2004).
[4] T. A. A. Adcock, P. H. Taylor, S. Yan, Q. W. Ma, and P. A. E. M. Janssen, Proceedings of the Royal Society A: Mathematical, Physical and Engineering Sciences **467**, 3004 (2011).
[5] N. Mori, P. C. Liu, and T. Yasuda, Ocean Engineering **29**, 1399 (2002).
[6] B. Baschek and J. Imai, Oceanography **24**, 158 (2011).
[7] E. Pelinovsky and C. Kharif, *Extreme Ocean Waves*, edited by E. Pelinovsky and C. Kharif (Springer International Publishing, Cham, 2016) pp. 1–236.
[8] A. Chabchoub, N. P. Hoffmann, and N. Akhmediev, Physical Review Letters **106**, 204502 (2011).
[9] A. Chabchoub, N. Hoffmann, M. Onorato, and N. Akhmediev, Physical Review X **2**, 2 (2012).
[10] M. L. McAllister, S. Draycott, T. A. Adcock, P. H. Taylor, and T. S. Van Den Bremer, Journal of Fluid Mechanics **860**, 767 (2018).
[11] G. Xu, A. Chabchoub, D. E. Pelinovsky, and B. Kibler, Physical Review Research **2**, 33528 (2020).
[12] E. G. Charalampidis, J. Cuevas-Maraver, D. J. Frantzeskakis, and P. G. Kevrekidis, Romanian Reports in Physics **70**, 1 (2018).
[13] D. R. Solli, C. Ropers, P. Koonath, and B. Jalali, Nature **450**, 1054 (2007).
[14] J. M. Dudley, F. Dias, M. Erkintalo, and G. Genty, Nature Photonics **8**, 755 (2014).
[15] B. Frisquet, B. Kibler, P. Morin, F. Baronio, M. Conforti, G. Millot, and S. Wabnitz, Scientific Reports **6**, 1 (2016).
[16] A. Tikan, C. Billet, G. El, A. Tovbis, M. Bertola, T. Sylvestre, F. Gustave, S. Randoux, G. Genty, P. Suret, and J. M. Dudley, Physical Review Letters **119**, 33901 (2017).
[17] R. Höhmann, U. Kuhl, H. J. Stöckmann, L. Kaplan, and E. J. Heller, Physical Review Letters **104**, 1 (2010).
[18] M. S. Ruderman, European Physical Journal: Special Topics **185**, 57 (2010).
[19] R. Sabry, W. M. Moslem, and P. K. Shukla, Physics of Plasmas **19** (2012), 10.1063/1.4772058.
[20] A. S. Bains, B. Li, and L. D. Xia, Physics of Plasmas **21** (2014), 10.1063/1.4869464.
[21] R. E. Tolba, W. M. Moslem, N. A. El-Bedwehy, and S. K. El-Labany, Physics of Plasmas **22** (2015), 10.1063/1.4918706.
[22] M. Onorato, S. Residori, U. Bortolozzo, A. Montina, and F. Arecchi, Physics Reports **528**, 47 (2013).
[23] A. R. Osborne, in *Scattering* (Elsevier, Amsterdam, 2002) pp. 637–666.
[24] C. Sulem and P. Sulem, *The Nonlinear Schrödinger Equation: Self-Focusing and Wave Collapse*, edited by C. Sulem and P.-L. Sulem, Applied Mathematical Sciences, Vol. 139 (Springer New York, New York, NY, 2004).
[25] M. J. Ablowitz, B. Prinari, and A. D. Trubatch, *Discrete and Continuous Nonlinear Schrödinger Systems* (Cambridge University Press, 2003).
[26] D. H. Peregrine, The Journal of the Australian Mathematical Society. Series B. Applied Mathematics **25**, 16 (1983).
[27] E. G. Charalampidis, J. Lee, P. G. Kevrekidis, and C. Chong, Physical Review E **98**, 032903 (2018).
[28] N. Akhmediev and A. Ankiewicz, Physical Review E **83**, 046603 (2011).
[29] A. Ankiewicz, N. Akhmediev, and J. M. Soto-Crespo, Physical Review E **82**, 026602 (2010).
[30] X. Y. Wen and D. S. Wang, Wave Motion **79**, 84 (2018).
[31] Z. Yan and D. Jiang, Journal of Mathematical Analysis and Applications **395**, 542 (2012).
[32] A. Maluckov, N. Lazarides, G. Tsironis, and L. Hadžievski, Physica D: Nonlinear Phenomena **252**, 59 (2013).
[33] C. Hoffmann, E. Charalampidis, D. Frantzeskakis, and P. Kevrekidis, Physics Letters A **382**, 3064 (2018).
[34] J. Sullivan, E. G. Charalampidis, J. Cuevas-Maraver, P. G. Kevrekidis, and N. I. Karachalios, European Physical Journal Plus **135**, 1 (2020).
[35] D. Han, M. Westley, and S. Sen, Physical Review E **90**, 032904 (2014).
[36] R. Kashyap and S. Sen, arXiv preprint arXiv:2105.05028 (2021).
[37] A. Merkel, V. Tournat, and V. Gusev, Physical Review Letters **107**, 225502 (2011).
[38] H. Pichard, A. Duclos, J.-P. Groby, V. Tournat, and V. E. Gusev, Physical Review E **89**, 013201 (2014).
[39] J. Köpfler, T. Frenzel, M. Kadic, J. Schmalian, and M. Wegener, Physical Review Applied **11**, 034059 (2019).
[40] A. Ngapasare, G. Theocharis, O. Richoux, C. Skokos, and V. Achilleos, Physical Review B **102**, 054201 (2020).

[41] F. Allein, V. Tournat, V. E. Gusev, and G. Theocharis, Extreme Mechanics Letters **12**, 65 (2017).

[42] B. Dubus, N. Swinteck, K. Muralidharan, J. O. Vasseur, and P. A. Deymier, Journal of Vibration and Acoustics, Transactions of the ASME **138** (2016), 10.1115/1.4033457.

[43] B. Deng, P. Wang, Q. He, V. Tournat, and K. Bertoldi, Nature Communications **9**, 3410 (2018).

[44] Q. Zhang, O. Umnova, and R. Venegas, Physical Review E **100**, 062206 (2019).

[45] H. Yasuda, Y. Miyazawa, E. G. Charalampidis, C. Chong, P. G. Kevrekidis, and J. Yang, Science Advances **5**, eaau2835 (2019).

[46] B. Deng, C. Mo, V. Tournat, K. Bertoldi, and J. R. Raney, Physical Review Letters **123**, 24101 (2019).

[47] C. Sugino, Y. Xia, S. Leadenham, M. Ruzzene, and A. Erturk, Journal of Sound and Vibration **406**, 104 (2017).

[48] D. Beli, J. R. Arruda, and M. Ruzzene, International Journal of Solids and Structures **139-140**, 105 (2018).

[49] A. T. Karttunen and J. N. Reddy, International Journal of Solids and Structures **204-205**, 172 (2020).

[50] Y. T. Wang, X. N. Liu, R. Zhu, and G. K. Hu, Scientific Reports **8**, 1 (2018).

[51] X. Yin, S. Zhang, G.-K. Xu, L.-Y. Zhang, and Z.-Y. Gao, Extreme Mechanics Letters **36**, 100668 (2020).

[52] L.-Y. Zhang, X. Yin, J. Yang, A. Li, and G.-K. Xu, Composites Science and Technology **207**, 108740 (2021).

[53] H. Fang, T. S. Chang, and K. W. Wang, Smart Materials and Structures **29** (2020), 10.1088/1361-665X/ab524e.

[54] P. P. Pratapa, P. Suryanarayana, and G. H. Paulino, Journal of the Mechanics and Physics of Solids **118**, 115 (2018).

[55] M. Peyrard and A. R. Bishop, Physical Review Letters **62**, 2755 (1989).

[56] T. Dauxois, M. Peyrard, and A. R. Bishop, Physical Review E **47**, 684 (1993).

[57] D. Chevizovich, D. Michieletto, A. Mvogo, F. Zakiryanov, and S. Zdravković, Royal Society Open Science **7**, 200774 (2020).

[58] G. Y. Lee, C. Chong, P. G. Kevrekidis, and J. Yang, Journal of the Mechanics and Physics of Solids **95**, 501 (2016).

[59] B. Kresling, in *Materials Research Society Symposium Proceedings*, Vol. 1420 (2012) pp. 42–54.

[60] L. L. Howell, S. P. Magleby, and B. M. Olsen, *Handbook of Compliant Mechanisms* (John Wiley and Sons, 2013).

[61] V. F. Nesterenko, *Dynamics of Heterogeneous Materials* (Springer New York, 2001).

[62] G. Huang, Z.-P. Shi, and Z. Xu, Physical Review B **47**, 14561 (1993).

[63] C. Chong and P. G. Kevrekidis, *Coherent Structures in Granular Crystals: From Experiment and Modelling to Computation and Mathematical Analysis*, 1st ed. (Springer International Publishing, 2018).

[64] A. Jeffrey and T. Kawahara, *Asymptotic methods in nonlinear wave theory*, Applicable mathematics series (Pitman Advanced Pub. Program, Boston, 1982).

[65] S. Manakov, Journal of Experimental and Theoretical Physics **38**, 248 (1973).

[66] M. Haelterman, A. P. Sheppard, and A. W. Snyder, Optics Letters **18**, 1406 (1993).

[67] M. Haelterman and A. P. Sheppard, Physics Letters A **194**, 191 (1994).

[68] M. Haelterman and A. Sheppard, Physical Review E **49**, 3376 (1994).

[69] S. Stalin, R. Ramakrishnan, M. Senthilvelan, and M. Lakshmanan, Physical Review Letters **122**, 043901 (2019).

[70] R. Ramakrishnan, S. Stalin, and M. Lakshmanan, Physical Review E **102**, 042212 (2020).

[71] Y. S. Kivshar and G. P. Agrawal, *Optical Solitons: From Fibers to Photonic Crystals* (Elsevier, 2003) pp. 1–540.

[72] F. Baronio, A. Degasperis, M. Conforti, and S. Wabnitz, Physical Review Letters **109** (2012), 10.1103/PhysRevLett.109.044102.

[73] M. Bertola and A. Tovbis, Communications on Pure and Applied Mathematics **66**, 678 (2013).

[74] C. Chong, Y. Wang, D. Maréchal, E. G. Charalampidis, M. Molerón, A. J. Martínez, M. A. Porter, P. G. Kevrekidis, and C. Daraio, New Journal of Physics **23**, 043008 (2021).

[75] See Supplemental Note 1 contains further details of prototypical model, which includes Ref. [76].

[76] H. Yasuda, T. Tachi, M. Lee, and J. Yang, Nature Communications **8**, 962 (2017).